Synthetic microlensing maps of the Galactic bulge

E. Kerins, A.C. Robin, D.J. Marshall

Mon. Not. R. Astron. Soc. **396,** 1202–1210 (2009) doi:10.1111/j.1365-2966.2009.14791.x

Synthetic microlensing maps of the Galactic bulge

E. Kerins,[1⋆] A. C. Robin[2] and D. J. Marshall[2,3]

[1] *Jodrell Bank Centre for Astrophysics, The University of Manchester, Oxford Road, Manchester M13 9PL*
[2] *Observatoire de Besançon Institut UTINAM, Université Franche-Comté, CNRS-UMR 6213, BP 1615, 25010 Besançon Cedex, France*
[3] *Département de Physique, de Génie Physique et d'Optique et Centre de Recherche en Astrophysique du Québec, Université Laval, Québec, QC, G1K 7P4, Canada*

Accepted 2009 March 18. Received 2009 March 13; in original form 2008 May 29

ABSTRACT

We present synthetic maps of the microlensing optical depth, event rate and time-scales over an area of 195 deg^2 towards the Galactic bulge. The maps are computed from stellar population synthesis catalogues generated from the Besançon Galaxy Model, which comprises four stellar populations and a three-dimensional extinction map calibrated against the Two-Micron All-Sky Survey. The microlensing maps have a resolution of 15 arcmin, corresponding to the angular resolution of the extinction map. We compute optical depth and event rate maps for all resolved sources above $I = 19$, for unresolved 'difference image' (DIA) sources magnified above this limit, and for bright 'standard candle' sources. The resulting optical depth and rate contours are dominated by extinction effects, in contrast to previous theoretical microlensing maps, and underscore the need to include realistic extinction modelling. Comparison of optical depth measurements to the Besançon model favours a bulge mass of $\sim 1.3 \times 10^{10}\,\mathrm{M}_{\odot}$. The microlensing maps exhibit a systematically higher optical depth for DIA sources, in line with experimental determinations. The predicted contours of the microlensing rate show very good correspondence with the field positions of the OGLE-III survey, illustrating how they have been optimized to maximize microlensing yields. We also show how the event distribution for hypothetical J and K-band microlensing surveys, using existing ground-based facilities such as VISTA, UKIRT or CFHT, would be much less affected by extinction, especially in the K band. The near infrared provides a substantial sensitivity increase over current I-band surveys and a more faithful tracer of the underlying stellar distribution, something which upcoming variability surveys such as Vista Variables in the Via Lactea (VVV) will be able to exploit. Only a fraction of current data sets has been employed for Galactic structure studies and more detailed models will be required to fully exploit the full catalogue of current survey samples, not to mention those coming online in the near future. Synthetic population modelling offers a promising way forward towards high-precision Galactic structure studies using microlensing.

Key words: gravitational lensing – stars: statistics – Galaxy: bulge – Galaxy: structure.

1 INTRODUCTION

Several microlensing survey teams have been monitoring millions of stars over a large region of the Galactic bulge for more than a decade (Sumi et al. 2003; Popowski et al. 2005; Hamadache et al. 2006; Sumi et al. 2006). These surveys have detected thousands of events and the combined detection rate of the OGLE-III and MOA-II surveys is currently around 800 unique events per year. The microlensing optical depth, that is the instantaneous number of ongoing microlensing events per source star, is a key measurable for these surveys and provides an important constraint on the bulge surface mass density. Its dependence upon direction provides, in principle, a powerful probe of the three-dimensional geometry of the bulge stellar mass distribution. The microlensing rate is governed both by the optical depth and the average event duration, the latter quantity being sensitive to the velocities of the lenses and sources and also to the lens mass function.

To date several measurements have been made of the optical depth along different directions. The MOA surveys (Sumi et al. 2003) find an optical depth from difference image analysis (DIA) of 28 events of $\tau_{\rm dia} = 2.59^{+0.84}_{-0.64} \times 10^{-6}$ for bulge and disc sources around Baade's Window ($l \simeq 1^{\circ}$, $b \simeq -3^{\circ}.9$). Most recent measurements of the optical depth have been based upon a restricted subset of red clump giant (RCG) stars, which act approximately as standard candles and are known to be confined to the bulge. From a sample of 42 RCG events, the Massive Astrophysical Compact Halo Objects survey (MACHO) collaboration (Popowski et al. 2005) measures a standard candle optical depth of

⋆E-mail: Eamonn.Kerins@manchester.ac.uk

$\tau_{sc} = 2.17^{+0.47}_{-0.38} \times 10^{-6}$ at ($l = 1.^{\circ}5$, $b = -2.^{\circ}7$). The OGLE-II survey (Sumi et al. 2006) reports a value of $\tau_{sc} = 2.55^{+0.57}_{-0.46} \times 10^{-6}$ determined from 32 RCG events in the direction ($l = 1.^{\circ}2$, $b = -2.^{\circ}7$). The largest single sample analysed to date involves 120 RCG events obtained by the Expérience de Recherche d'Objects Sombres (EROS-2) experiment (Hamadache et al. 2006), from which it measured the optical depth over a large region, including $\tau_{sc} = (2.42 \pm 0.47) \times 10^{-6}$ within ($-3.^{\circ}5 < b < -1.^{\circ}4$). EROS-2 also reports an optical depth gradient with latitude $|b|$ of $\mathrm{d}\tau_{sc}/\mathrm{d}|b| \simeq (0.78 \pm 0.27) \times 10^{-6}\,\mathrm{deg}^{-1}$ at $b = -2.^{\circ}7$, in line with similar gradient determinations by MACHO and OGLE-II.

Despite initial disagreement, optical depth measurements from RCG sources are now largely in accord with recent theoretical models (Evans & Belokurov 2002; Han & Gould 2003; Wood & Mao 2005) and support the existence of a bar-like bulge which is oriented 10°–20° from the Sun – Galactic Centre line. However, RCG events represent less than 10 per cent of all bulge microlensing events. A major limitation to the study of the remaining events comes from the current simplicity of theoretical models. A fully developed model must account for the line-of-sight distribution of the sources in both the disc and bulge components. This distribution is a function not only of the underlying density models but also of the experimental sensitivity, the source luminosity function and the distribution of dust. The latter factor is particularly problematic for studies of the spatial distribution of events since extinction varies strongly with sky position. Until recently realistic three-dimensional extinction maps were unavailable.

In this paper, we present the first microlensing optical depth and event rate maps to incorporate a realistic three-dimensional extinction map. The map was developed by Marshall et al. (2006) as part of the Besançon Galaxy Model (Robin et al. 2003). In Section 2, we briefly overview the Besançon Model including how the three-dimensional dust map was generated. In Section 3, we describe how we set up the optical depth and rate calculations. In Section 4, we present maps of optical depth and event rate for current *I*-band microlensing surveys, as well as for a hypothetical near-infrared survey which, as we show, would be much less affected by dust. We end with a discussion in Section 5.

2 THE BESANÇON GALAXY MODEL

The Besançon Galaxy Model is a simulation tool aimed at testing galaxy evolution scenarios by comparing stellar distributions predicted by these scenarios with observational constraints, such as photometric star counts and kinematics. A complete description of the model ingredients can be found in Robin et al. (2003). We summarize here the model's principal features which are relevant to the present analysis. In particular, we do not discuss the details of the metallicity of each population as the microlensing quantities do not depend directly on them.

2.1 Stellar populations

The model assumes that stars are created from gas following a star formation history and an initial mass function (IMF); stellar evolution follows evolutionary tracks. To reproduce the overall galaxy formation and evolution, we distinguish four populations of different ages and star formation history.

(i) The spheroid population is described in Robin, Reylé & Crézé (2000) as a single burst population of age 14 Gyr. Its kinematics are modelled by a triaxial velocity distribution with dispersions (σ_U, σ_V, σ_W) = (131, 106, 85) km s^{-1}. Its density in the central regions is small compared to other populations and it is therefore only a marginal contributor to the optical depth.

(ii) The thick disc is formed from stars born about 11–12 Gyr ago in a short period of time as implied by recent metallicity determinations for this population. We also assume a single burst for simplicity. For the thick disc, star formation occurred from the gas already settled in the disc. Kinematics, deduced from observational constraints (Ojha et al. 1996, 1999), imply that it has undergone a merging event shortly after the disc formation (Robin et al. 1996), increasing the disc thickness and giving a higher velocity dispersion and scaleheight. The IMF, density distribution and local normalization are constrained by star counts (Reylé & Robin 2001).

(iii) The bulge population is present in the centre of the Galaxy and extends to about 3–4 kpc. Its age is around 10 ± 2 Gyr. The population is modelled from Bruzual & Charlot (2003) population synthesis, as a single burst and a Salpeter IMF. This population reflects a triaxial bar distribution, as determined by Picaud & Robin (2004) from near-infrared star counts. The angle of the major axis of the bulge with the Sun-Galactic Centre axis is found to be 11.°3. The scalelengths are 1.590, 0.424 and 0.424 kpc. The total bulge mass is $2.05 \times 10^{10}\,\mathrm{M}_{\odot}$. The bulge velocity ellipsoid is modelled with dispersions (σ_U, σ_V, σ_W) = (113, 115, 100) km s^{-1} and a pattern speed of 53 km s^{-1} kpc^{-1}.

(iv) For the thin disc, a standard evolutionary model is used to compute the disc population, comprising an IMF, a star formation rate (SFR) and a set of evolutionary tracks, as described in Haywood, Robin & Crézé (1997b) and references therein. The disc population is assumed to evolve during 10 Gyr, with multiple periods of star formation creating seven distinct age populations. A set of IMF slopes and SFRs are tentatively assumed and then tested against star counts. The tuning of disc parameters against relevant observational data has been described in Haywood, Robin & Crézé (1997a) and Haywood et al. (1997b). A revised IMF has been adjusted to agree with the most recent *Hipparcos* results: the age–velocity dispersion relation is from Gomez et al. (1997), the local luminosity function from Jahreiß & Wielen (1997), giving an IMF slope $\alpha = 1.5$ in the low mass range (0.5–0.08 $\mathrm{M}_{\odot}$), in good agreement with Kroupa (2001). The scaleheight has been computed self-consistently using the potential via the Boltzmann equation. The local dynamical mass is taken from Crézé et al. (1998).

Stellar remnants are also included in the model, though their role in the optical depth analysis is only indirect in contributing to the overall mass of lensing stars and in limiting the overall mass normalization for visible stars which act as microlens sources; the microlensing optical depth is insensitive to the stellar or remnant mass function of the lenses (see Section 3). We assume all white dwarfs to be of type DA and use evolutionary tracks and atmosphere models from Bergeron, Leggett & Ruiz (2001), complemented by Chabrier (1999) for the very cool end, applicable to the halo. No brown dwarfs are included in the present model. All simulated stars are single stars.

The evolutionary model fixes the distribution of stars in the space of intrinsic parameters: effective temperature, gravity, absolute magnitude, mass and age. These parameters are converted into colours in various systems through stellar atmosphere models.

The detectability of stars computed in the simulations is subject to interstellar extinction as described below.

2.2 Extinction distribution

Marshall et al. (2006) have built a three-dimensional model of the distribution of the dust in the inner Galaxy ($|l| < 100^{\circ}, |b| < 10^{\circ}$)

from an analysis of the 2MASS survey (Skrutskie et al. 2006) using the Besançon Galaxy Model. By comparing the observed reddened stars to the unredenned simulated stars of the Besançon model, they were able to calculate the extinction as a function of distance for any given line of sight in the Galaxy. The extinction along a line of sight is that which minimizes the chi-squared difference between the $J - K_s$ colour distributions of the observed and simulated stars. The final map has an angular resolution of 15 arcmin and a distance resolution of 100–500 pc. Better angular resolutions are possible but at the cost of reducing the resolution in distance.

Having established the Galactic model we now turn our attention to its microlensing properties.

3 OPTICAL DEPTH EVALUATION

The optical depth is one of the primary measurables which can be obtained from statistical analyses of microlensing events. It depends only on the distribution and mass normalization of the source and lens stellar populations and is therefore potentially a very powerful probe of Galactic structure. The optical depth to a source at distance S is (Paczyński 1986)

$$\tau = \int_0^S \frac{\pi R_{\rm E}^2}{M} \rho(L)\, {\rm d}L, \tag{1}$$

where L is the observer lens distance, M is the lens mass, ρ is the lens mass density and $R_{\rm E} = [4GML(S-L)/c^2S]^{1/2}$ is the Einstein radius of the lens, with G and c having their usual meaning.

An evaluation of τ must involve an average over the observed source population. Such an average must take account of, among other factors, the survey sensitivity. Current microlensing surveys such as OGLE-III and MOA-II are observing in the I band and are typically capable of 4 per cent photometry at approximately $I = 19$ (cf. fig. 5 of Udalski et al. 2002). We therefore adopt this limit for our I-band calculations. We will also consider a hypothetical near-infrared microlensing survey observing in the J or K band. We assume it to be capable of 4 per cent photometry at $J = 18$ and $K = 17$ for comparison. Such a survey could be conducted with facilities such as UKIRT, VISTA or CFHT and, as we will see, would have the advantage of being much less affected by dust than the I-band surveys. One survey which will be capable of detecting bulge microlensing events in the near-infrared is the Vista Variables in the Via Lactea (VVV) survey,[1] which is scheduled to commence in 2009 on the recently completed VISTA telescope in Chile.

We start by computing optical depths according to equation (1) over a three-dimensional grid of source positions (l, b, S), where l and b are Galactic coordinates. For the lenses, we employ the same underlying mass density distributions as are used in the Besançon Model simulations. We then use the Besançon population synthesis program to generate synthetic catalogues of millions of source stars. The catalogues cover the region $|l| < 9\overset{\circ}{.}75$, $|b| < 5^\circ$, giving a total area of 195 deg^2. Each catalogue probes 3239 lines of sight to give a map resolution of $15 \times 15\,{\rm arcmin}^2$, which is the limit of the resolution of the dust map. Finally, we interpolate the optical depth grid at the position of each synthetic source to arrive at a source-averaged optical depth, τ, for each line of sight.

We consider three different optical depth quantities. The first is $\tau_{\rm res}$, which is the optical depth averaged over all 'resolved' sources, i.e. those which at baseline are brighter than the assumed survey limit of $I = 19$, $J = 18$ or $K = 17$. The second optical depth quantity is $\tau_{\rm dia}$ which represents the average over all DIA sources, i.e. those which at peak magnification are brighter than the assumed survey limit. DIA sources can be significantly fainter than the survey limit at baseline and so our simulated source catalogues go 4 mag fainter than our assumed survey limits. We weight the optical depth contribution of each DIA source by min $(1, u_{\rm t}^2)$, where $u_{\rm t}$ is the largest impact parameter, in units of $R_{\rm E}$, which allows the event to be detected above the survey limit. This is necessary because, at any instant, only a fraction $u_{\rm t}^2$ of unresolved sources are expected to be magnified sufficiently to be detectable as events. Many recent optical depth measurements have been based upon a subset of events involving bright RCG sources, which are approximate standard candles. We therefore compute a third optical depth quantity, $\tau_{\rm sc}$, where τ is averaged over a subset of bright 'standard candle' sources located around the clump giant region of the colour–magnitude diagram. Our standard candle source selection has

$$I_0 < \min[I_{0,\rm RC}^* + 1, 9(V-I)_0 + I_{0,\rm RC}^* - 5.5], \tag{2}$$

where subscript 0 denotes dereddened magnitude and the red clump magnitude $I_{0,\rm RC}^* = 14.66 - 0.033l$, with l the Galactic longitude expressed in degrees. This prescription follows the 'extended red clump' selection algorithm of Sumi et al. (2006), where we have adopted a weighted linear fit to the zero-point corrected red clump magnitude values, $I_{0,\rm RC}^*$, listed in table 2 of Sumi et al. (2006) for Galactic latitudes $b < 0$.

In addition to the optical depth, we also compute the event rate using the proper motion information generated by the simulations. To obtain lens proper motions, we run another simulation where the magnitude limits are relaxed (in practise a magnitude range of -99 to 99 is adopted), so that all stars and remnants are included. The relative proper motion μ, lens Einstein radius $R_{\rm E}$ and Einstein crossing time $t_{\rm E} = R_{\rm E}/\mu L$ are then computed for all lens and source combinations where the lens distance $L < S$. From this, the average event duration $\langle t_{\rm E}\rangle$ is computed by weighting each time-scale by $\mu L R_{\rm E}$ (or $u_{\rm t}\mu L R_{\rm E}$ for DIA sources). Finally, the rate is obtained as $\Gamma = 2\tau/\pi\langle t_{\rm E}\rangle$.

We depart slightly from the model of Robin et al. (2003) by adopting a Galactocentric distance of $R_0 = 8$ kpc for all of our simulations.

4 OPTICAL DEPTH AND EVENT RATE MAPS

We present the results from Section 3 in two forms. First, as straightforward I-band maps of optical depth, and secondly we present I-band maps of the event rate. In the last part of this section, we also present near-infrared microlensing maps.

4.1 Maps of the Optical Depth

In Fig. 1, we present I-band optical depth maps for resolved sources ($\tau_{\rm res}$), DIA sources ($\tau_{\rm dia}$) and bulge 'standard candle' sources ($\tau_{\rm sc}$). The optical depth is indicated both by the grey-scale level and by the contours, which are set at 1, 2 and 4×10^{-6}.

The number of simulated stars made within each $0.25 \times 0.25\,{\rm arcmin}^2$ cell ranges from a handful for regions of high extinction, up to $N \sim 15\,000$ for low-extinction regions of the inner bulge. The simulation error on the computed optical depth is $\Delta\tau/\tau = \langle t_{\rm E}\rangle^{-1}\sqrt{\langle t_{\rm E}^2\rangle/N} \simeq 2/\sqrt{N}$ (Han & Gould 1995). Typically, $N \sim 2000$ per cell for the standard candle or resolved star sources wherever $\tau \gtrsim 10^{-6}$, and $N \sim 5000$ per cell for the DIA sources (though some DIA sources carry small weighting). Hence, τ is evaluated to an accuracy of at worst a few per cent wherever $\tau \gtrsim 10^{-6}$. In regions of low source density at the periphery of the maps where

[1] http://www2.astro.puc.cl/VVV/

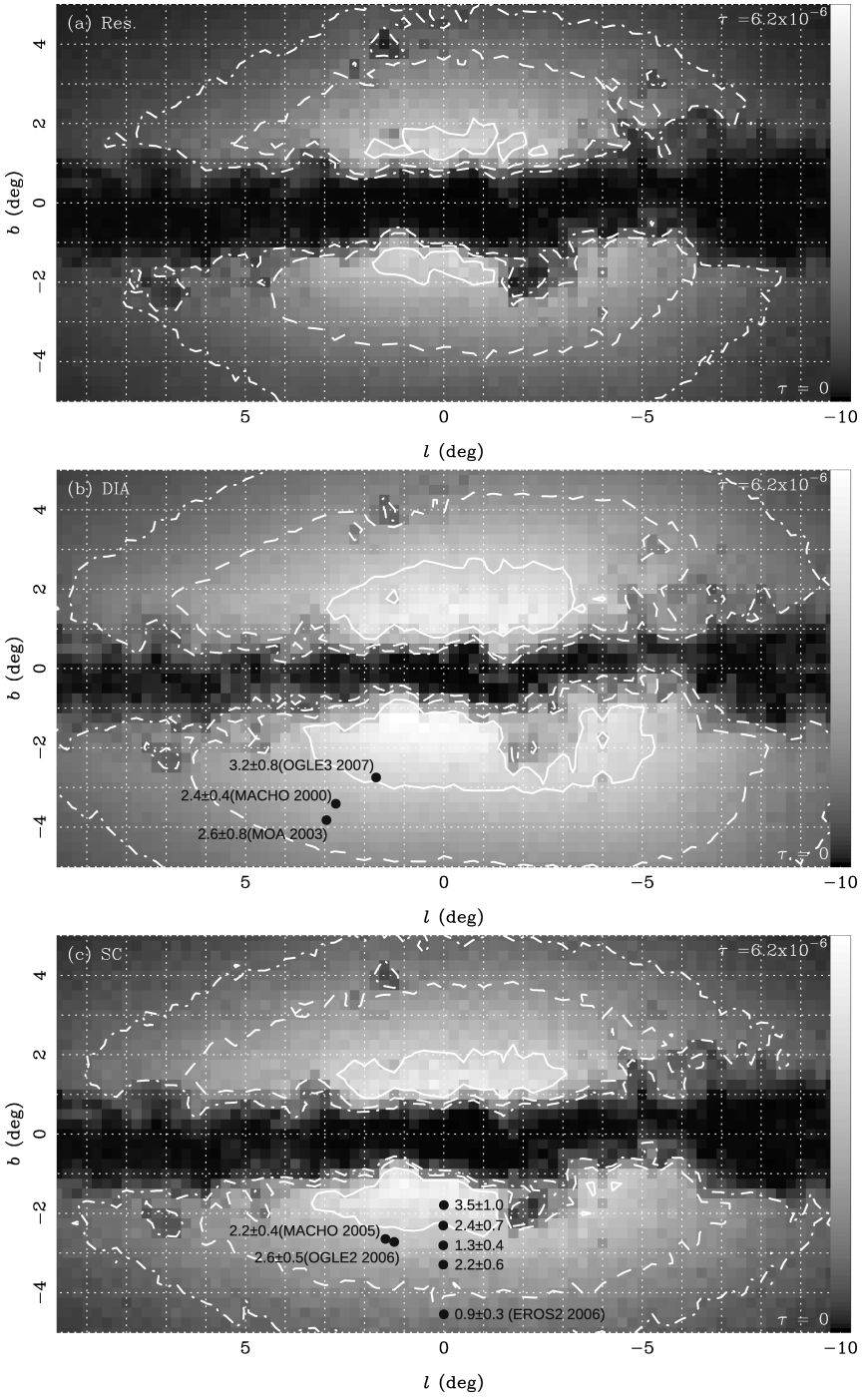

Figure 1. *I*-band optical depth grey-scale maps. (a) The optical depth, $\tau_{\rm res}$, to all sources brighter then $I = 19$ at baseline. (b) The optical depth, $\tau_{\rm dia}$, to all sources brighter than $I = 19$ at peak magnification. (c) The optical depth, $\tau_{\rm sc}$, to 'standard candle' sources as defined by equation (2). Solid, dashed and dot–dashed contours indicate optical depths of 4, 2 and 1×10^{-6}, respectively. The low-optical depth towards the Galactic plane is due to the high extinction in this region. The grey-scale range is given by the bar to the right of each plot and is normalized to a maximum value of 6.2×10^{-6} for all panels. Also shown in panels (b) and (c) are DIA and clump giant optical depth measurements by MACHO (Alcock et al. 2000; Popowski et al. 2005), MOA (Sumi et al. 2003), OGLE2 (Sumi et al. 2006), EROS2 (Hamadache et al. 2006) and OGLE3 (Kozlowski 2007). For EROS2, a series of measurements over various latitudes *b* are shown at $l = 0^\circ$, though they are averaged over a wide range of Galactic longitudes.

there may be only a few hundred simulated sources [corresponding to $\tau \lesssim \mathcal{O}(10^{-7})$] the error is closer to 10–15 per cent.

The most obvious distinguishing feature of these maps from previously published predictions is the irregularity of the contour line shapes. This is a direct consequence of the effect of dust. At latitudes $|b| \lesssim 1^\circ$, the very high column density of dust results in a negligible optical depth because only relatively nearby sources are detectable and these have an intrinsically small lensing optical depth from equation (1). The region of high extinction centred at $l \simeq -2^\circ$, $b \simeq -2^\circ$ is also clearly evident from the microlensing optical depth distribution. Away from the Galactic plane, the optical depth contours are smoother and comparable to previous models (e.g. Wood

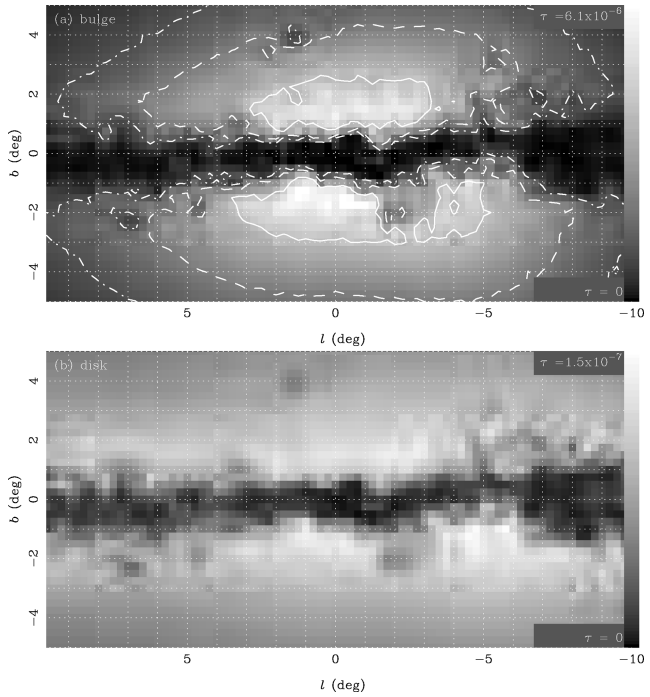

Figure 2. The *I*-band DIA optical depth maps separately for (a) spheroid+bulge and (b) thin+thick disc lenses. Contours and grey-scales in (a) are as for Fig. 1, whilst the grey-scale range in (b) is 40 times lower than in (a) for clarity of display. The sum of the panels (a) and (b) corresponds to panel (b) in Fig. 1.

& Mao 2005). In particular, the predicted 'standard candle' optical depth gradient south of the plane and away from regions of high dust density is $\mathrm{d}\tau_{\rm sc}/\mathrm{d}|b| \simeq 0.8 \times 10^{-6}\,\mathrm{deg}^{-1}$, in very good agreement with measurements from RCG sources (Popowski et al. 2005; Sumi et al. 2006; Hamadache et al. 2006). Fig. 2 shows the separate contributions to the DIA optical depth of lenses in the bulge and spheroid (panel a) and lenses in the thin and thick disc (panel b). The optical depth is strongly dominated by bulge lenses, especially as the disc in the Besançon model possesses a central hole where the disc density diminished within the bar region.

In the absence of the dust, the central hotspot in the optical depth and event density maps would be located at negative Galactic longitude due to the higher optical depth towards the far side of the bar (e.g. Wood & Mao 2005). However, this is much more difficult to see in the presence of the dust distribution. When the dust is included the *I*-band optical depth peaks in a localized hotspot centred around $l \simeq 0.^{\circ}5$, $b \simeq -1.^{\circ}5$ with a value of 5.2×10^{-6} for resolved sources, 6.2×10^{-6} for DIA sources and 5.9×10^{-6} for standard candle sources. Evidence for such a hotspot comes from the distribution of events within the EROS-2 event sample (Hamadache et al. 2006) and the OGLE-II Early Warning System (EWS; Udalski et al. 2003). The EROS-2 bright star event sample clearly shows the greatest contribution from the measured optical depth coming from events in this area (cf. fig. 14 in Hamadache et al. 2006). In Section 4.2, we discuss the distribution of events from the OGLE-III EWS.

One interesting feature which emerges from Fig. 1 is that the DIA optical depth $\tau_{\rm dia}$ appears slightly less prone to the effects of extinction, with a notably narrower avoidance zone due to dust near the Galactic plane. Also interesting are differences in the optical depth between the three measures for specific locations. For example, at Baade's Window ($l = 1^{\circ}$, $b = -3.^{\circ}9$), both $\tau_{\rm res}$ and $\tau_{\rm sc}$ yield optical depths $\tau \simeq 2 \times 10^{-6}$ whilst $\tau_{\rm dia} \simeq 3 \times 10^{-6}$. This is consistent with the tendency of surveys to yield higher optical depth values from DIA events samples.

However, the model is clearly not perfect. Comparison of the optical depth maps with recent measurements (Alcock et al. 2000; Sumi et al. 2003, 2006; Popowski et al. 2005; Hamadache et al. 2006; Kozlowski 2007) indicates that the Besançon model overestimates by about 60 per cent the optical depth of bulge standard candle sources. This may simply reflect the relatively high bulge mass of $2.05 \times 10^{10}\,\mathrm{M}_{\odot}$ employed in the Besançon model. A bulge mass of $1.3 \times 10^{10}\,\mathrm{M}_{\odot}$, which was derived by Dwek et al. (1995) from their photometric analysis, would provide a better match to the optical depth measurements. However, another contributing factor may be that the extinction map effectively saturates in higher extinction regions ($A_V > 20$) where the 2MASS *K*-band sensitivity is relatively low. Consequently, the extinction may be underestimated in regions where $A_V > 15$ (Schultheis et al. 2009). Either way, a new bulge model for the Besançon simulation is in preparation and microlensing data should provide a useful consistency check for it.

Another important factor when comparing predicted and observed optical depths is the photometric cuts used to define the source sample from which the optical depth is computed. Differences between $\tau_{\rm res}$, $\tau_{\rm dia}$ and $\tau_{\rm sc}$ highlight the need for theoretical optical depth calculations to consider carefully the photometric characteristics of individual survey selections. Whilst survey detection efficiency calculations may account for factors such as colour selections, they none the less assume some underlying luminosity function for the microlensing sources, which may not necessarily be the same as assumed in theoretical calculations.

4.2 Maps of the event rate

Fig. 3 shows an *I*-band map of the average event duration for resolved sources with $I < 19$, computed from the proper motions predicted by the Besançon model. The event duration is sensitive to lens and source kinematics as well as the lens mass function. Away from the central bulge region the time-scale contours flare outwards towards higher latitudes, something also seen in the time-scale maps of Evans & Belokurov (2002). The time-scales for the Besançon model are typically slightly longer than those computed by Evans & Belokurov (2002). For events closer to the plane extinction effects mean that they are dominated by relatively nearby disc lens/disc source microlensing where the time-scales are determined by the relatively small disc velocity dispersion. Another notable aspect of Fig. 3 is the sharper flaring of the time-scale contours at

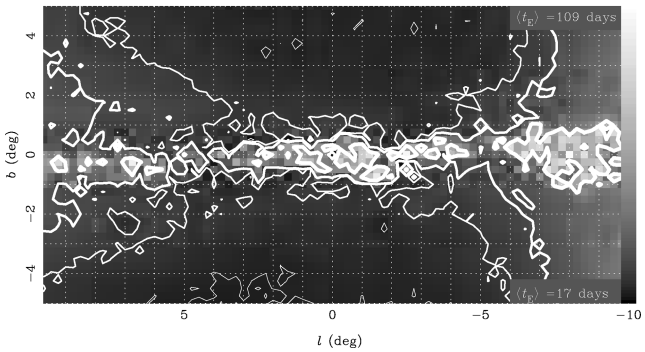

Figure 3. The distribution of average event durations $\langle\, t_{\rm E} \rangle$ for resolved sources with baseline magnitudes $I < 19$. From the thinnest to the thickest contours, the average durations are 20, 25, 30 and 60 d, respectively.

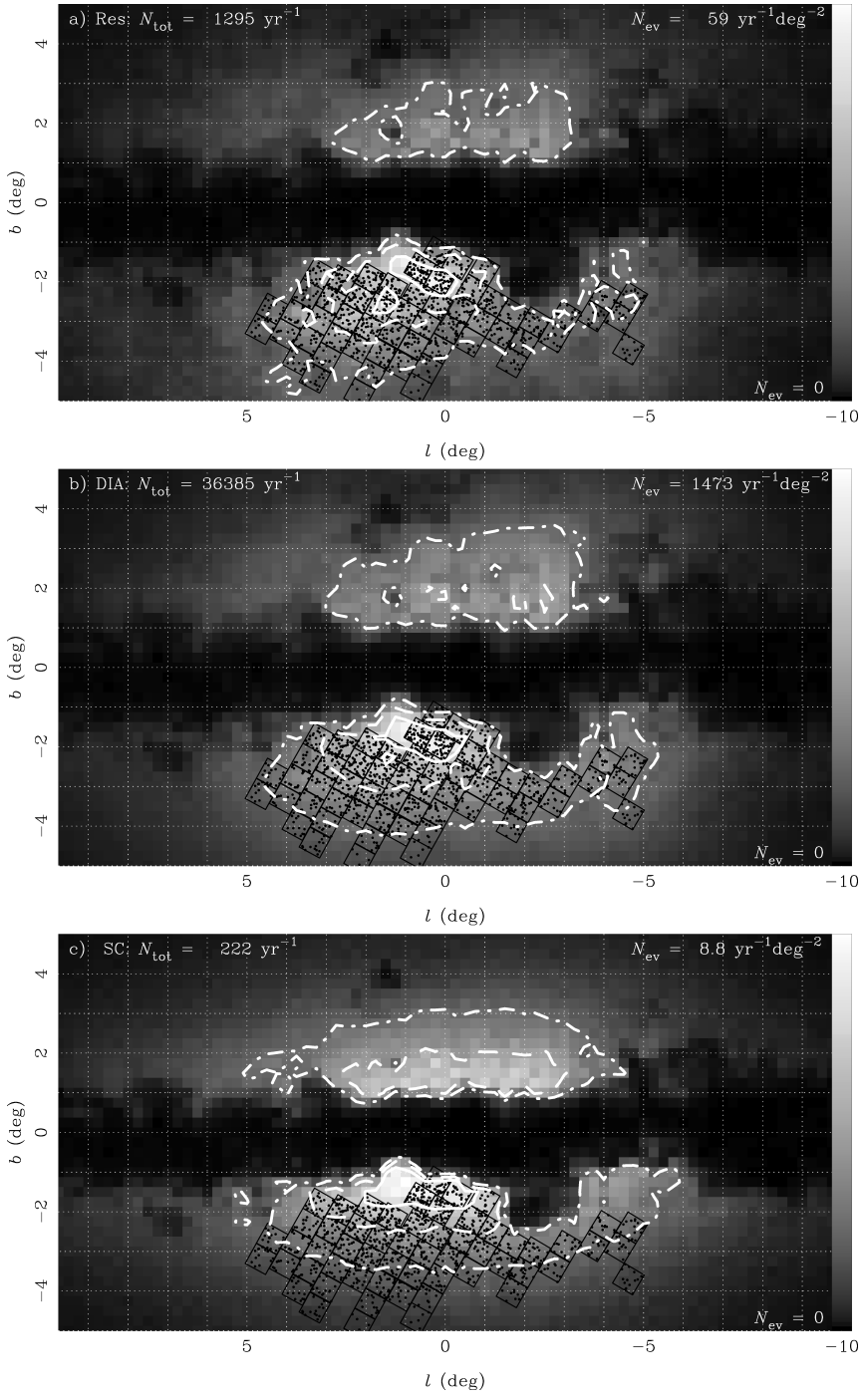

Figure 4. I-band grey-scale maps of $N_{\rm ev}$, the microlensing event rate per year per square degree. Panels (a), (b) and (c) correspond to the cases plotted in Fig. 1. The contour levels indicate 25, 50 and 75 per cent of the peak rate. The panels also show 57 OGLE-III field locations (black squares) along with 1407 events with Einstein radius crossing times $10 < t_{\rm E}/{\rm d} < 100$ detected by the OGLE EWS between 2005 and 2008 (black dots). Note that the grey-scale normalization is different in each of the plots. The number $N_{\rm tot}$ denotes the total event rate across the whole 195 deg^2 region for a survey with perfect detection efficiency.

$l \lesssim -5^\circ$ than for positive longitudes $l \gtrsim 5^\circ$. The main reason for this is the bar geometry. Whilst the bulk of the optical depth is due to bulge lenses the sources are drawn from both the disc and bulge for the near-bar lenses at positive l, but primarily from just the bulge for the far-bar lenses at negative l. Differences in kinematics between the disc and bulge sources therefore affect differently the shape of the average time-scale contours at positive and negative longitudes.

Fig. 4 displays maps of the event rate obtained by dividing the optical depth maps by their respective time-scale distribution maps. The grey-scale map and contours in the plots in Fig. 4 trace the event rate with contour levels corresponding to 25, 50 and 75 per cent of the maximum rate. The total rate over the whole simulated area is given by $N_{\rm tot}$ in the upper-left corner of each panel. Fig. 4 also shows the positions of 57 OGLE-III fields together with 1407 events detected within these fields between 2005 and 2008 by the

OGLE-III EWS.[2] We have excluded events with Einstein radius crossing times $t_E < 10$ d in order to suppress the bias induced by the fact that some of the OGLE-III fields are monitored several times per night whilst others are monitored nightly. Additionally, we exclude long-duration events with $t_E > 100$ d so as to minimize the risk of tracing localized kinematic structures that may not be represented in our maps.

For all the *I*-band maps, there is a predicted hot-spot in the event rate at around $l \simeq 1^\circ, b \simeq -2^\circ$.The maps clearly indicate that one expects many more events south of the plane than north of it, supporting the current strategy of the survey teams in focussing predominately on the southern side of the plane.

Interestingly, the distribution of OGLE-III EWS alerted events also shows hotspots in the regions predicted by the model, and generally the model correlates quite well with the alert event distribution. This is particularly evident by the way in which the 25 per cent-level rate contour traces the periphery of the OGLE-III field locations for resolved and DIA sources. This is precisely what one would expect assuming that OGLE has positioned its fields in order to maximize the event discovery rate. Just as for the optical depth contours the rate contours are strongly affected by the presence of dust, though the contours for standard candle sources appear to be best at tracing the bar profile, as one might expect since the colour cuts are designed to select primarily bulge sources.

The OGLE-III EWS sensitivity approximates to that of panel (a) in Fig. 4, though some events involve fainter sources. Currently, the OGLE-III EWS detects around 500 events per year over an area of around 20 deg^2. Fig. 4 shows that the OGLE-III fields are well optimized to the highest yielding regions and therefore succeed in detecting the bulk of the events within the simulated area. The predicted rate of resolved sources for the whole area of 195 deg^2 is around 1300 yr^{-1}. Allowing for the fact that OGLE does not observe the whole year round, that one might expect the EWS detection efficiency to be $\sim$50 per cent and that the OGLE-III fields do not cover the whole simulated area, the predicted rate seems reasonably consistent with the EWS observed rate. A more robust quantitative comparison cannot be made without knowing the EWS detection efficiency. Interestingly, the overall rate of events with DIA sources is a factor of 27 larger than the rate from resolved sources. This suggests that there are many more events which peak within the OGLE-III sensitivity. However, in practice, the large bulk of these events would not have sufficient signal to noise across the rise and fall of the light curve to allow them to be reliably distinguished as microlensing events.

Since the detection efficiency of the EWS is completely uncalibrated we must be wary of drawing quantitative conclusions from a comparison with its event yield, but on the face of it the model appears capable of reproducing clumpy features seen in the observed event distribution. One exception may be at $l \simeq 1^\circ$, $b \simeq -1.^\circ5$ where the model predicts a strong *I*-band microlensing signature but which is not covered by the OGLE survey, which has been optimized over 17 seasons in order to concentrate on high event yield locations. None the less, with sufficiently sophisticated models, there is clearly the exciting prospect of using the large available samples of microlensing events to constrain fine structure in the underlying Galactic structure, once the data detection efficiency is known.

[2] http://www.astrouw.edu.pl/~ogle/ogle3/ews/ews.html

4.3 Near-infrared microlensing

We finish by considering the potential impact of microlensing surveys in the near-infrared (Gould 1995; Evans & Belokurov 2002). Specifically, we consider the event density in the *J* and *K* bands for resolved sources, assuming a survey capable of 4 per cent photometry at $J = 18$ and $K = 17$. Such a survey could be performed using the wide-field infrared cameras available on telescopes such as UKIRT, VISTA or CFHT. Indeed the VVV survey is scheduled to commence on VISTA in 2009 as an ESO Public Survey. The VVV will survey some 520 deg^2 of the disc and bulge, primarily in the *K* band, over five seasons, with at least one season of almost nightly monitoring from which a substantial number of microlensing events should be detected.

The top, middle and bottom panels in Fig. 5 show, respectively, the *I*-band map (also shown in the top panel of Fig. 4), the *J*-band

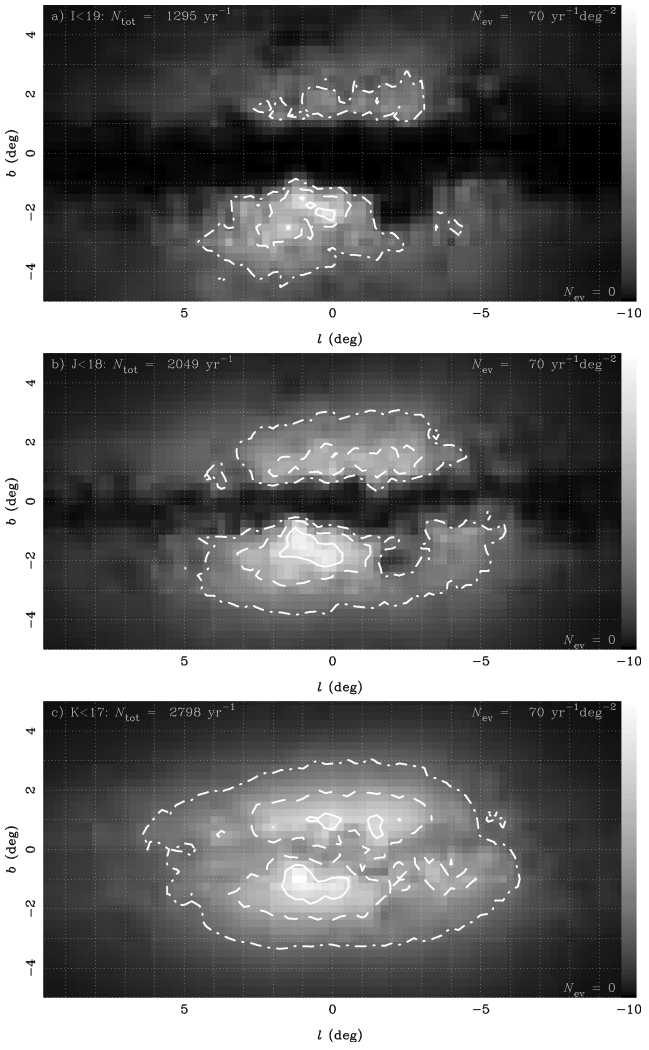

Figure 5. A comparison of *I*, *J* and *K*-band maps of the event rate. The greyscale in each map is normalized to a peak density of 70 events yr^{-1} deg^{-2}. Panel (a) is a reproduction of panel (a) in Fig. 4 whilst panels (b) and (c) show the event density in the *J* and *K* bands, respectively, for all sources brighter than $J = 18$ and $K = 17$. Such a near-infrared microlensing survey could be undertaken with telescopes such as UKIRT, VISTA or CFHT. The advantage of lesser extinction, particularly in the *K* band, is clearly evident. The contour levels indicate rates of 17.5, 35 and 52.5 events yr^{-1} deg^{-2}, assuming perfect detection efficiency.

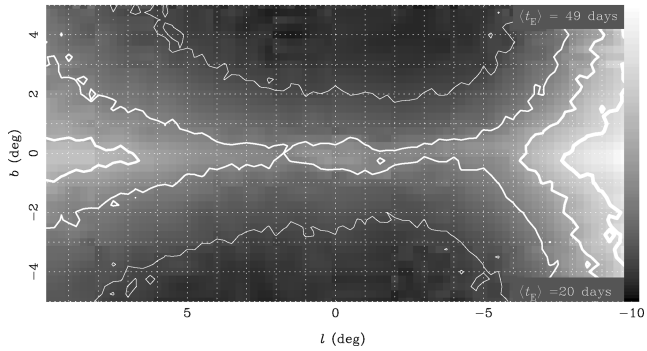

Figure 6. The distribution of K band average event durations $\langle t_{\rm E}\rangle$ for resolved sources with baseline magnitudes $K < 17$. From the thinnest to the thickest contours, the average durations are 24, 30, 36 and 42 d, respectively.

map and the K-band map of the event rate for resolved sources (i.e. using $\tau_{\rm res}$). The grey-scale levels of the maps are matched to an event density of 70 events yr^{-1} deg^{-2} for direct comparison and the contours indicate 25, 50 and 75 per cent of its peak level. The advantage of observing in the near-infrared is very clear. First, the effects of extinction are greatly reduced, especially in K, so that the overall event rate is more than a factor of 2 higher than in the I band. The relative smoothness of the K-band rate contours also means that the events more faithfully trace the shape of the underlying mass distribution. These two factors alone mean that a K-band survey like VVV would have powerful advantages over I-band surveys for Galactic structure studies.

However, another important advantage of observing in J or K is that the northern hemisphere also becomes an attractive target for microlensing studies. In particular, the region around $|l| \lesssim -1^\circ$, $b \simeq 1^\circ$ exhibits a reasonably strong microlensing signature in the K band, and a respectable signal even in the J band. The significance of this is that this region includes the far side of the bar at negative l. The ability to survey both the near and far sides of the bar would allow the separate microlensing contributions of the disc and bulge to be separated, as the far bar should have a significantly higher disc optical depth than the near bar.

Fig. 6 shows the distribution of average event durations $\langle t_{\rm E}\rangle$ for K-band microlensing. The contours are rather smoother than for the optical case in Fig. 3 and do not include long-time-scale events near the plane, due to the much lessened effects of extinction. The effect of the bar geometry on the asymmetry of the contour distribution is therefore clearer even at low latitudes.

5 DISCUSSION

We have used a synthetic population synthesis model of the Galaxy to construct maps of the microlensing optical depth and event rate. The Besançon Model employs a three-dimensional extinction map and allows optical depth and rate maps to be computed for individual passbands, and for the maps to adopt sophisticated cuts in source colour and magnitude.

We have computed I-band microlensing maps for three distinct event samples: stars which at baseline are resolved at $I < 19$ ($\tau_{\rm res}$), comparable to current microlensing survey limits, stars which reach $I < 19$ at peak magnification ($\tau_{\rm dia}$), and sources which are selected using colour cuts similar to those used to define standard candle samples such as RCGs ($\tau_{\rm sc}$). The structure in the resulting optical depth maps is dominated by the effects of extinction towards the Galactic pane, and demonstrates a much stronger microlensing signal south of the Galactic plane, which is where most of the survey effort is being concentrated. We find that $\tau_{\rm dia}$ tends to be less affected by the dust and is systematically higher than $\tau_{\rm res}$ ir $\tau_{\rm sc}$. The Besançon model tends to overpredict the optical depth, probably owing to its relatively high bulge mass of $2.05 \times 10^{10}\,{\rm M}_\odot$. A mass nearer $1.3 \times 10^{10}\,{\rm M}_\odot$ would likely give a good fit to current microlensing data.

We find good correlation between event rate maps and the location of 1407 events detected by the OGLE-III EWS. A direct quantitative comparison cannot be made since the efficiency of the EWS is unknown. However, the model successfully predicts the region of highest event yield as seen by both the OGLE-III and EROS-2 surveys, suggesting that the large-scale features of the model are correct. We also find good agreement between the predicted optical depth gradient with latitude and that determined by microlensing surveys.

We also investigate the potential of near-infrared microlensing surveys by computing the event rate in the J and K bands. The K band in particular is extremely promising in circumventing the worst effects of interstellar dust. K-band rate contours more faithfully trace the underlying structure of the bulge and also allow both the near- and far-bar to be probed for microlensing. Comparison of near- and far-bar microlensing samples would allow the separate microlensing signatures of disc and bulge lenses to be decoupled, providing additional constraints on Galactic models. Upcoming near-infrared variability surveys, such as VVV, therefore have the potential to provide excellent microlensing samples for Galactic structure studies.

The number of discovered microlensing events is now around 5000, and yet so far only a few hundred have been analysed for Galactic structure studies. Whilst theoretical models which ignore extinction (or assume it to be smooth) can be compared reasonably successfully with samples of $\sim$100 events, they likely will be inadequate for dealing with samples of several thousand events, where fine structure may start to become evident. An accurate calibration of the stellar mass budget in the inner Galaxy is also a vital pre-requisite to evaluating the allowable mass budget of dark matter in the inner Galaxy. The analysis of microlensing data sets can therefore provide important indirect constraints on the dark matter halo profile. We believe that synthetic modelling provides an excellent way forward for such work. By fully exploiting the large and expanding catalogues of microlensing samples, synthetic modelling provides the potential for microlensing to be used as a high-precision probe of Galactic structure.

ACKNOWLEDGMENTS

EK is supported by an Advanced Fellowship from the Science and Technology Facilities Council. DJM is supported by the Natural Sciences and Engineering Research Council of Canada through its SRO programme. EK wishes to thank Shude Mao for helpful discussions. EK and ACR would like to thank James Binney for hosting a European Science Foundation Workshop on Galaxy modelling, from which came the idea for this work. We thank the anonymous referee for several suggestions which have helped to improve on an earlier version of this manuscript.

REFERENCES

Alcock C. et al., 2000, ApJ, 541, 734
Bergbush P., VandenBerg D., 1992, ApJS, 81, 163
Bergeron P., Leggett S. K., Ruiz M. T., 2001, ApJS, 133, 413

Bruzual G., Charlot S., 2003, MNRAS, 344, 1000
Chabrier G., 1999, ApJ, 513, L103
Crézé M., Chereul E., Bienaymé O., Pichon C., 1998, A&A, 329, 920
Dwek E. et al., 1995, ApJ, 445, 716
Evans N. W., Belokurov V., 2002, ApJ, 567, 119
Gomez A. E., Grenier S., Udry S., Haywood M., Meillon L., Sabas V., Sellier A., Morin D., 1997, in Perryman M. A. C., Bernacca P. L., Battrick B., eds., ESA SP-402. ESA, Noordwijk, p. 621
Gould A., 1995, ApJ, 446, L71
Hamadache C. et al., 2006, A&A, 454, 185
Han C., Gould A., 1995, ApJ, 449, 521
Han C., Gould A., 2003, ApJ, 592, 172
Haywood M., Robin A. C., Crézé M., 1997a, A&A, 320, 440
Haywood M., Robin A. C., Crézé M., 1997b, A&A, 320, 428
Jahreiß H., Wielen R., 1997, in Perryman M. A. C., Bernacca P. L., Battrick B., eds., ESA SP-402. ESA, Noordwijk, p. 675
Kozlowski S., 2007, PhD Thesis, Univ. Manchester
Kroupa P., 2001, MNRAS, 322, 231
Marshall D. J., Robin A. C., Reylé C., Schultheis M., Picaud S., 2006, A&A, 453, 635
Ojha D. K., Bienaymé O., Robin A. C., Crézé M., Mohan V., 1996, A&A, 311, 456
Ojha D. K., Bienaymé O., Mohan V., Robin A. C., 1999, A&A, 351, 945
Paczyński B., 1986, ApJ, 304, 1
Picaud S., Robin A. C., 2004, A&A, 428, 891
Popowski P. et al., 2005, ApJ, 631, 879
Reylé C., Robin A. C., 2001, A&A, 373, 886
Robin A. C., Haywood M., Crézé M., Ojha D. K., Bienaymé O., 1996, A&A, 305, 125
Robin A., Reylé C., Crézé M., 2000, A&A, 359, 103
Robin A., Reylé C., Derrière S., Picaud S., 2003, A&A, 409, 523
Schultheis M., Sellgren K., Ramirez S., Stolovy S., Ganesh S., Glass I. S., Girardi L., 2009, A&A, 495, 157
Skrutskie M. F. et al., 2006, AJ, 131, 1163
Sumi T. et al., 2003, ApJ, 591, 204
Sumi T. et al., 2006, ApJ, 636, 240
Udalski A. et al., 2002, AcA, 52, 217
Udalski A. et al., 2003, AcA, 53, 291
Wood A., Mao S., 2005, MNRAS, 362, 945

This paper has been typeset from a TEX/LATEX file prepared by the author.